NANO-G ACCELEROMETER USING GEOMETRIC ANTI-SPRINGS

B.A. Boom[1], A. Bertolini[1], E. Hennes[1], R.A. Brookhuis[2], R.J. Wiegerink[2],
J.F.J. van den Brand[1,3], M.G. Beker[4], A. Oner[1], and D. van Wees[1]
[1]Nikhef, Amsterdam, THE NETHERLANDS
[2]University of Twente, Enschede, THE NETHERLANDS
[3]VU University, Amsterdam, THE NETHERLANDS
[4]Innoseis, Amsterdam, THE NETHERLANDS

ABSTRACT

We report an ultra-sensitive seismic accelerometer with nano-g sensitivity, using geometric anti-spring technology. High sensitivity is achieved by an on-chip mechanical preloading system comprising four sets of curved leaf springs that support a proof-mass. Using this preloading mechanism, stiffness reduction up to a factor 26 in the sensing direction has been achieved. This increases the sensitivity to acceleration by the same factor. The stiffness reduction is independent of the proof-mass position, preserving the linear properties of the mechanics and due to its purely mechanical realization, no power is consumed when the accelerometer is in its preloaded state. Equivalent acceleration noise levels below $2\,\mathrm{ng}/\sqrt{\mathrm{Hz}}$ have been demonstrated in a 50 Hz bandwidth, using a capacitive half-bridge read-out.

INTRODUCTION

The recent first direct detection of gravitational waves by the LIGO/Virgo Collaboration [1] encouraged the interest to even further improve the bandwidth and sensitivity of ground-based detectors. Low-frequency sensitivity (2-20 Hz) for future gravitational wave detectors will be limited by Newtonian noise, caused by direct gravitational force fluctuations on the detector's suspended test masses due to local seismic vibrations, air density fluctuations and human activity. Even building such a detector in a seismically quiet location is, although crucial, not enough to sufficiently suppress this noise. The most promising measure to battle seismic Newtonian noise is to use dense arrays of highly sensitive seismometers to monitor the local seismic fields and applying subtraction schemes to cancel detector noise correlated to them [2]. It is in this context that the ultra-sensitive MEMS accelerometer presented here is developed.

GEOMETRIC ANTI-SPRINGS

For any accelerometer, the sensitivity to acceleration below resonance is proportional to $1/\omega_0^2 = m/k$. When the total sensor noise performance is limited by the ability to sense the proof-mass position, it is therefore beneficial to lower the accelerometer's natural frequency, ω_0, i.e. by increasing the mass and/or decreasing the stiffness. In practice, lower bounds in natural frequency are set by the very limited proof-mass sizes available in MEMS sensors and by the difficulty in maintaining sufficiently high stiffness ratios between the sensitive and non-sensitive degrees of freedom.

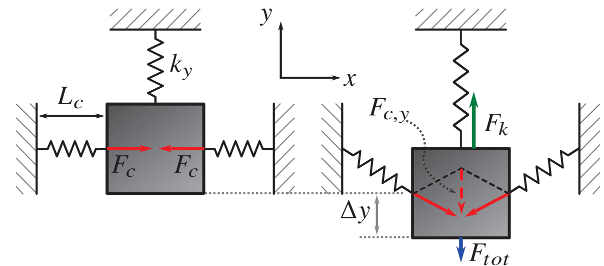

Figure 1: Conceptual illustration of GAS effect. Left: proof-mass in equilibrium position with lateral preload F_c. Right: Proof-mass in displaced state. Most of F_k is cancelled by $F_{c,y}$.

In the presented device, geometric anti-spring (GAS) technology is used to lower the natural frequency after fabrication. GAS technology is a concept originating from the gravitational wave detector community, where it is used to lower the resonance frequency of large seismic isolation filters [3]. For the first time, this concept is miniaturized and integrated into a MEMS accelerometer. Compared to the state of the art in ultra-low noise accelerometers, using geometric anti-spring technology results in low self-noise using a much smaller proof-mass, significantly reducing the chip area [4].

The anti-spring effect is illustrated in figure 1. By introducing a static compression force, F_c, orthogonal to the sensing direction (y-direction), any proof-mass displacement along the sensitive axis will give rise to a force $F_{c,y} = -2F_c \cdot \Delta y/L_c$. This force cancels part of the restoring force introduced by the suspension springs, $F_k = k_y \cdot \Delta y$, and effectively lowers the total stiffness. Changing F_c will alter the stiffness in the sensing direction as desired. The stiffness indicated with k_y need not be physically separated from the loading springs, it merely represents the suspension stiffness in the sensitive direction. In the device presented here, the springs used to introduce the static load, also define k_y.

DESIGN

Figure 2(a) shows an overview of the total MEMS device. The central proof-mass is suspended by curved leaf springs at the four corners. The proof-mass position is sensed through 2 sets of variable gap type capacitor banks as shown

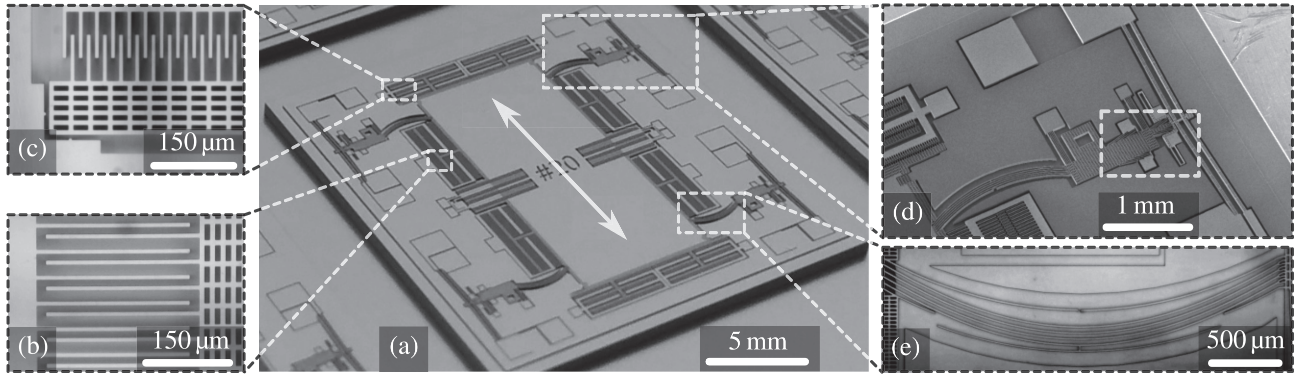

Figure 2: (a) Photograph of a full bare sensor die with detailed zooms of: (b) the variable gap sensing capacitors, (c) the variable overlap actuation capacitors, (d) one of the curved leaf spring suspensions along with its compression mechanism, and (e) one of the suspension spring sets in compressed state. A detailed view of the dashed box in (d) is shown in figure 3.

in inset (b). The capacitance of these banks changes differentially with the proof-mass position. Comb drive actuators shown in inset (c) are available for electrostatic actuation. Details on these structures can be found in table 1.

One of the spring suspensions is shown in its compressed state in figure 2(e). The left sides of the four leaf springs are attached to the proof-mass, while the right sides are connected to a linearly guided block that can be seen in inset (d). The springs are surrounded by etching guards that protect the spring sidewalls during the DRIE process. These do not bend with the springs and serve no purpose during sensor operation.

Figure 3 shows the mechanism that is used to load the springs. V-beam type electro-thermal actuators (ETAs) [5] are used to generate the mN range force needed to load the springs. The central part of one of these actuators is shown on the right side of the photograph. When a current is fed through this highly doped silicon beam, it expands and the central part moves left, pushing the linearly guided block connected to the leaf spring suspension with it.

The initial position of the pawls connected to this block with respect to the anti-reverse teeth is shown in inset 1 [6]. This structure makes sure that the guided block can only move left. When the pawls reach the state in inset 2, the ETAs are withdrawn, but the block cannot move back with it, because of the anti-reverse pawls. On withdrawing the ETAs, a second set of anti-reverse pawls close to the ETAs snaps to the next tooth, overcoming the limited range of motion of the ETAs for subsequent compression steps. Now the ETAs are engaged again until the guided block reaches the position shown in inset 3. Note that using two sets of pawls connected to the linearly guided block enables using a step size that is half of the minimum tooth size defined by the DRIE process and/or lithography. For this design, a step size of 5 µm was chosen. This stepping process can be repeated until the last step is reached in inset 6. At this point, the shuttle has traveled 35 µm to the left and the ETAs exert an estimated total compression force of approximately

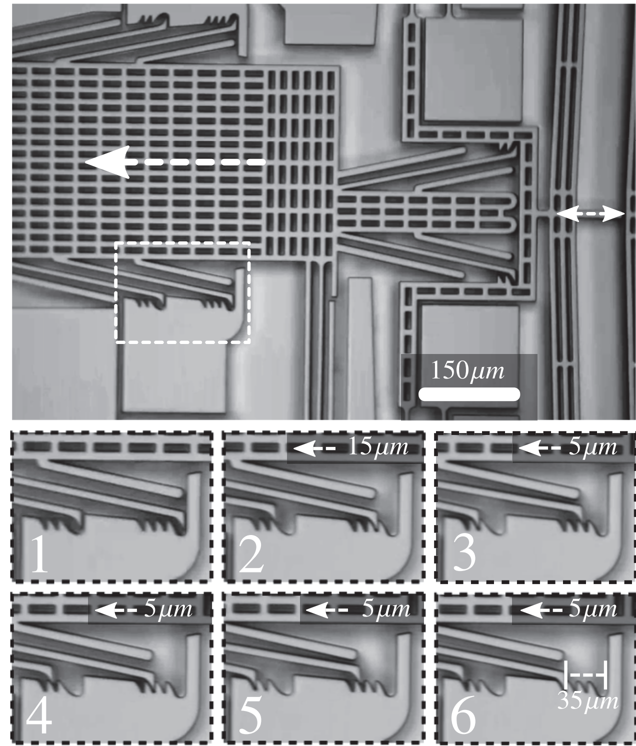

Figure 3: Top: Photograph of a preloading mechanism. The V-beam actuator is shown on the right. By repeatedly pumping the actuator, the linearly guided block on the left can be stepped forward with large force over a 35 µm range. Bottom: Photographs of dashed box for the six different steps.

Parameter	Type I	Type II
Proof-mass	32.9 mg	12.7 mg
f_0, uncompressed	102 Hz	184 Hz
f_0, compressed	28.1 Hz	36 Hz
Capacitive sensing gap	8 µm	8 µm
Actuation capacitor gap	7 µm	7 µm
Total sensing capacitance	13 pF	15 pF

Table 1: Key device parameters

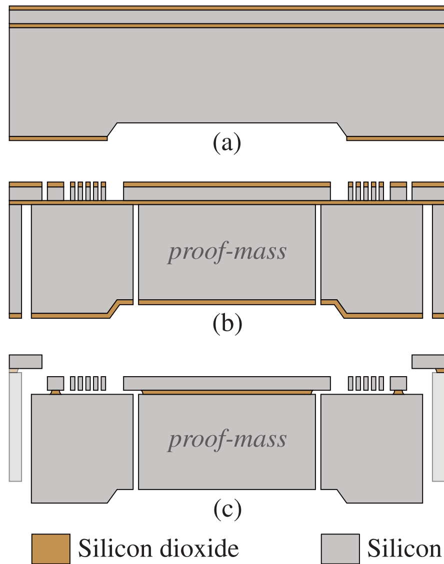

Figure 4: Fabrication process outline (see text).

14 mN on the anti-reverse structure. Note that the preloading is an irreversible, one-time procedure: after compression, the ETAs are withdrawn and the compression force is maintained mechanically, consuming no power during sensor operation.

Thanks to a symmetric sensor design, any compression of an opposite pair of suspension springs will not change the proof-mass equilibrium position. Moreover, the resulting reduction in effective stiffness is practically independent of the proof-mass position and the mechanical system therefore remains linear. This contrasts with systems where a negative stiffness is introduced by means of an electrostatic transducer. Here the negative stiffness is highly non-linear and stability issues arise.

FABRICATION

The accelerometer is realized using a single SOI wafer process. The SOI wafer has a 50 µm thick device layer, a 4 µm buried oxide layer and a 400 µm thick handle layer. All silicon is highly P-doped. The process flow outline is shown in figure 4. The region of the handle layer where the proof-mass will be formed is etched to a depth of 50 µm using KOH, both to protect the proof-mass during processing and handling, and to ensure free motion during operation. The springs, their preloading system and the capacitive readout structures are realized in the device layer by deep reactive ion etching (DRIE). The proof-mass is realized by DRIE of the handle layer (fig. 4(b)). Finally, the buried oxide layer is etched in vapor-HF, which releases the proof-mass such that it is only supported by its springs. In this step, the complete sensor is also released from its surrounding frame (fig. 4(c)), resulting in a dry and vibration free release process [7, 8]. Mechanical stops are incorporated in the design, to prevent excessive displacement of the proof-mass in all directions once the proof-mass is released.

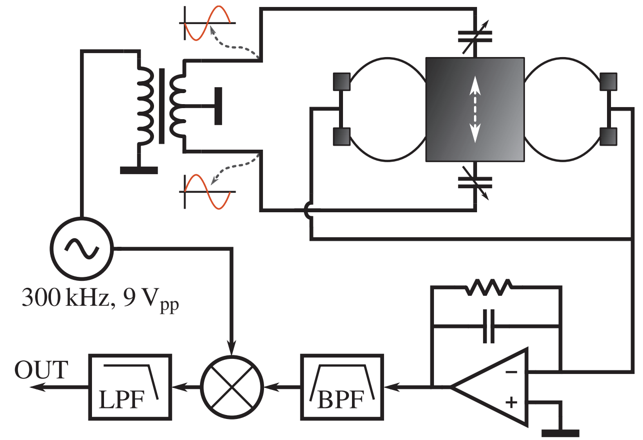

Figure 5: Schematic description of the position sensing scheme used to read the acceleration signal.

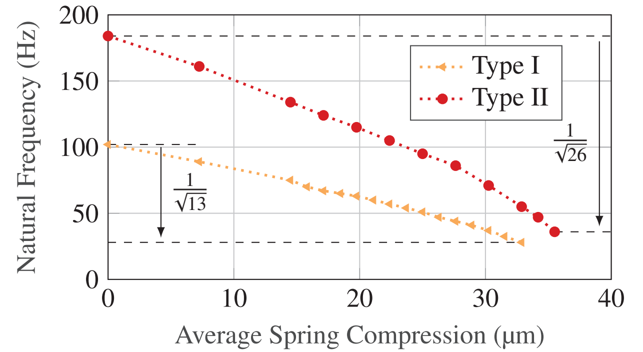

Figure 6: Measured natural frequency versus spring compression. Stiffness reduction up to 26 times has been reached.

EXPERIMENTAL RESULTS

Figure 6 shows the accelerometer's natural frequency as a function of the average suspension spring compression distance for two different types of sensors of which the key parameters are shown in table 1. Stiffness reduction of up to 26 times has been demonstrated. The accelerometer's response increases with the same factor and this pushes down the equivalent acceleration noise floor due the the position sensing-system.

To measure the position of the sensor proof-mass, a discrete component capacitive half-bridge readout was used, as shown in figure 5. A 300 kHz, 9 V_{pp} differential sine wave was applied across the two MEMS sensing capacitors. An imbalance between the sensing capacitors due to proof-mass motion will cause a net current into the charge amplifier. The amplifier will keep the proof-mass at virtual ground while providing an output signal amplitude proportional to the difference in capacitance. A synchronous demodulator and a low-pass filter provide an output signal proportional to the proof-mass position.

Measuring the noise performance of an ultra-sensitive accelerometer is not straightforward, because of the constant

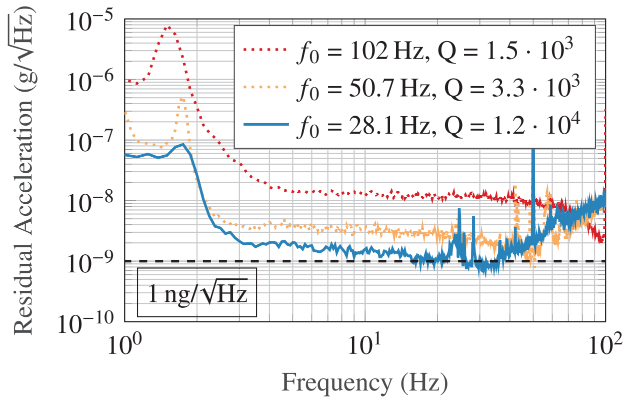

Figure 7: Sensor equivalent acceleration noise floor as a function of natural frequency. Low frequency signals are caused by motion of the vibration isolation table. Noise is dominated by the standard capacitive pick-off electronics and directly scales down with the square of the natural frequency.

presence of stimuli to the sensor due to seismic activity. Finding a natural location with seismic activity below 1 ng/$\sqrt{\text{Hz}}$ is hard, so instead an in-vacuum seismic isolation platform developed for the Virgo gravitational wave detector was used [9]. This platform consists of a cascade of one inverted and two regular pendula, connected through vertical motion filters. The isolator provides 100 dB of horizontal vibration attenuation and 70 dB attenuation of vertical motion at 3 Hz. At 10 Hz this figure improves to 140 dB and 100 dB respectively. The platform allows to relatively easily measure the accelerometer's equivalent acceleration noise floor above 3 Hz, but unfortunately gives no information on the sensor noise at lower frequencies, where the seismic motion propagates through the attenuation chain to the accelerometer.

By placing the sensor structure in vacuum, Brownian noise is reduced well below the electronic noise floor. Figure 7 shows the measured equivalent acceleration noise for three different preloading states of a Type I sensor. In all cases, this noise is dominated by the thermal noise from the charge-amplifier above 3 Hz and is measured in open-loop. The equivalent acceleration noise directly drops with the reduction in stiffness, because of the increased sensor sensitivity. In this case, the equivalent acceleration noise drops from about 13 ng/$\sqrt{\text{Hz}}$ at a natural frequency of 102 Hz to below 2 ng/$\sqrt{\text{Hz}}$ at 28.1 Hz. Equivalent noise levels start to rise above the accelerometer's natural frequency because of the decreasing response at higher frequencies.

CONCLUSION

A novel method to lower the noise floor of MEMS accelerometers was demonstrated. The system stiffness in the sensing direction can be reduced by preloading the suspension springs with a combination of an electro thermal V-beam actuator and a mechanical anti-reverse structure. Stiffness reduction up to a factor of 26 has been demonstrated. The accelerometer sensitivity is scaled up directly with this stiffness reduction factor and thereby lowers the equivalent acceleration noise floor caused by the electronics. Equivalent noise levels below 2 ng/$\sqrt{Hz}$ have been demonstrated in a 50 Hz bandwidth, using a discrete component capacitive half-bridge readout system.

ACKNOWLEDGEMENT

This work is part of the research programme of the Foundation for Fundamental Research on Matter (FOM), which is part of the Netherlands Organisation for Scientific Research (NWO).

REFERENCES

[1] B. P. Abbott *et al.*, "Observation of Gravitational Waves from a Binary Black Hole Merger," *Physical Review Letters*, vol. 116, no. 6, p. 061102, Feb. 2016.

[2] M. G. Beker, "Low-frequency sensitivity of next generation gravitational wave detectors," Ph.D. dissertation, Vrije U., Amsterdam, 2013.

[3] A. Bertolini *et al.*, "Seismic noise filters, vertical resonance frequency reduction with geometric anti-springs: a feasibility study," *Nuclear Instruments and Methods in Physics Research Section A: Accelerators, Spectrometers, Detectors and Associated Equipment*, vol. 435, no. 3, pp. 475 – 483, 1999.

[4] W. T. Pike *et al.*, "Design, fabrication and testing of a micromachined seismometer with nano-g resolution," in *TRANSDUCERS 2009 - 2009 International Solid-State Sensors, Actuators and Microsystems Conference*, June 2009, pp. 668–671.

[5] E. T. Enikov *et al.*, "Analytical model for analysis and design of v-shaped thermal microactuators," *Journal of Microelectromechanical Systems*, vol. 14, no. 4, pp. 788–798, Aug 2005.

[6] P. H. Pham *et al.*, "Single mask, simple structure micro rotational motor driven by electrostatic comb-drive actuators," *Journal of Micromechanics and Microengineering*, vol. 22, no. 1, p. 015008, 2012.

[7] T. Overstolz *et al.*, "A clean wafer-scale chip-release process without dicing based on vapor phase etching," in *Micro Electro Mechanical Systems, 2004. 17th IEEE International Conference on. (MEMS)*, 2004, pp. 717–720.

[8] I. Sari *et al.*, "A dicing free {SOI} process for {MEMS} devices," *Microelectronic Engineering*, vol. 95, pp. 121 – 129, 2012.

[9] M. G. Beker *et al.*, "State observers and kalman filtering for high performance vibration isolation systems," *Review of Scientific Instruments*, vol. 85, no. 3, 2014.

CONTACT

Boris Boom
borisb@nikhef.nl